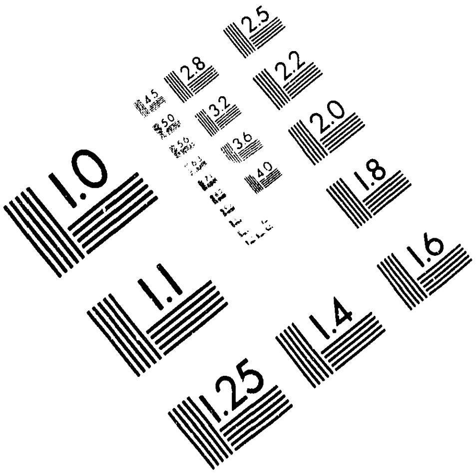

AIIM

Association for Information and Image Management

1100 Wayne Avenue, Suite 1100
Silver Spring, Maryland 20910

301/587-8202

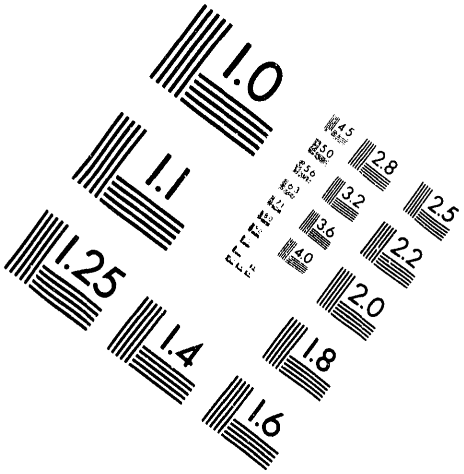

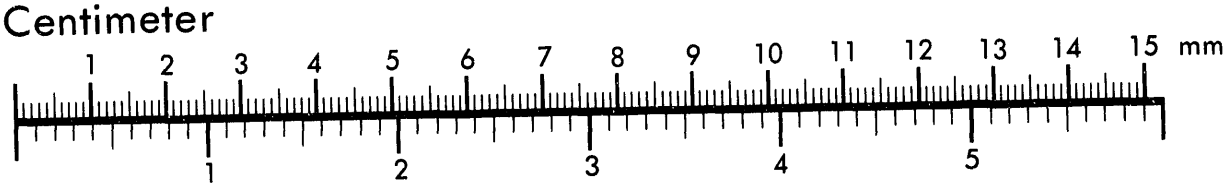

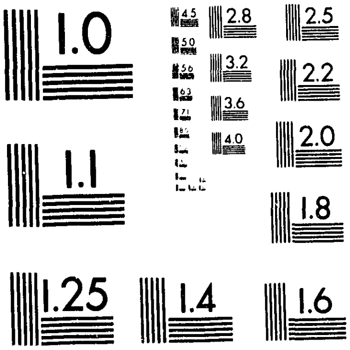

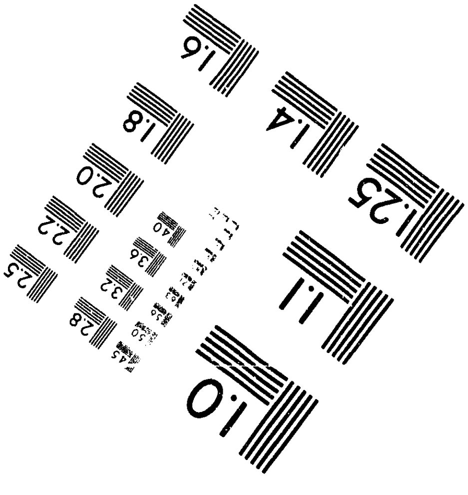

MANUFACTURED TO AIIM STANDARDS
BY APPLIED IMAGE, INC.

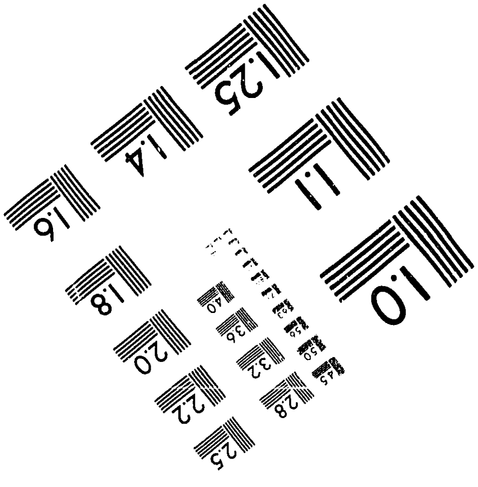

1 of 1

Fermi National Accelerator Laboratory

FERMILAB-Pub-93-097-A
May 12, 1993

Redshift distortions of galaxy correlation functions

J. N. FRY[1,2] AND ENRIQUE GAZTAÑAGA[1,3]

ABSTRACT

To examine how peculiar velocities can affect the 2-, 3-, and 4-point correlation functions, we evaluate volume-average correlations for configurations that emphasize and minimize distortions for four different volume-limited samples from each of the CfA, SSRS, and IRAS redshift catalogs. We present the results as the correlation length r_0 and power index γ of the 2-point correlation, $\bar{\xi}_2 = (r_0/r)^\gamma$, and as the hierarchical amplitudes of the 3- and 4-point functions, $S_3 = \bar{\xi}_3/\bar{\xi}_2^2$ and $S_4 = \bar{\xi}_4/\bar{\xi}_2^3$.

We find a characteristic distortion for $\bar{\xi}_2$: the slope γ is flatter and the correlation length is larger in redshift space than in real space; that is, redshift distortions "move" correlations from small to large scales. At the largest scales (up to $12\,h^{-1}$ Mpc), extra power in the redshift distribution is compatible with $\Omega^{4/7}/b \approx 1$; we find 0.53 ± 0.15, 1.10 ± 0.16 and 0.84 ± 0.45 for the CfA, SSRS and IRAS catalogs.

Higher order correlations $\bar{\xi}_3$ and $\bar{\xi}_4$ suffer similar redshift distortions, but in such a way that, within the accuracy of our analysis, the normalized amplitudes S_3 and S_4 are insensitive to this effect. The hierarchical amplitudes S_3 and S_4 are constant as a function of scale between 1–12 h^{-1} Mpc and have similar values in all samples and catalogues, $S_3 \approx 2$ and $S_4 \approx 6$, despite the fact that $\bar{\xi}_2$, $\bar{\xi}_3$, and $\bar{\xi}_4$ differ from one sample to another by large factors (up to a factor of 4 in $\bar{\xi}_2$, 8 for $\bar{\xi}_3$, and 12 for $\bar{\xi}_4$).

The agreement between the independent estimations of S_3 and S_4 is remarkable given the different criteria in the selection of galaxies and also the difference in the resulting range of densities, luminosities and locations between samples.

Subject Headings: Large-scale structure of the universe — galaxies: clustering

---

[1] NASA/Fermilab Astrophysics Center, Fermi National Accelerator Laboratory, Box 500, Batavia IL 60510-0500, USA

[2] Department of Physics, University of Florida, Gainesville FL 32611 USA

[3] Department of Physics, University of Oxford, Keble Road, Oxford OX1 3RH, England, UK

1 Introduction

Measurements of the galaxy 2-, 3-, and 4-point correlation functions, $\bar{\xi}_2$, $\bar{\xi}_3$, and $\bar{\xi}_4$, indicate that a hierarchical clustering structure, with $\bar{\xi}_J = S_J \, \bar{\xi}_2^{J-1}$, holds both in angular catalogs (Groth & Peebles 1977; Fry & Peebles 1978; Szapudi, Boschan, & Szalay 1992; Meiksin, Szapudi, & Szalay 1992) and in redshift catalogs (Bouchet, Davis, & Strauss 1993; Gaztañaga 1992), and both for IRAS and optically selected galaxies. The values obtained for the hierarchical amplitudes S_J do not completely agree between different analyses (see Table 8 below), and the question arises whether this is caused by redshift distortions or by differences in the techniques and selections employed, or arises from intrinsic differences in the samples.

Previous analyses of galaxy correlation functions have focused either on the projected distribution inferred from angular data or on the redshift distribution, but there are very few cases where both angular and redshift correlations have been estimated for the same sample (one notable exception for the 2-point correlation function is Davis & Peebles 1983). Deriving statistical properties from angular data requires many galaxies to compensate for the decrease in the projected amplitude, and introduces uncertainties from the selection function. With the addition of redshift information, the selection function is better known, but the total number of galaxies in redshift samples is usually orders of magnitude smaller because of the larger observational time required to take a single redshift. As a result, it is difficult to perform both analyses for a single catalog. In particular, for the 3- and 4-point correlation functions we do not know of any previous reference where both redshift and angular analyses are considered over identical data.

Statistics of galaxy clustering inferred from redshift data are likely to be distorted radially by peculiar velocities. One known effect is the "fingers of God": the large velocities in a tightly bound cluster disperse the apparent positions of galaxies along the line of sight, such that in the extreme, clusters appear as narrow needles pointed back at the observer. Since typical peculiar velocities are a few hundred kilometers per second, one might hope that by avoiding clusters or by looking on larger scales this effect could be rendered unimportant. However, fluctuations are also smaller on large scales and there are coherent streaming effects. Kaiser (1987) showed in perturbation theory that on large scales velocity distortions are of the same order as density fluctuations and distort large scale perturbation amplitudes by a factor $[1+f(\Omega)\cos^2\theta]$, where θ is the angle between the perturbation wave vector and the line of sight and $f(\Omega) \approx \Omega^{4/7}$. Averaged over a spherical volume, fluctuations in redshift space are thus enhanced by a factor $[1+f(\Omega)/3]$. Thus, we expect possible redshift distortions on all scales.

The effect on higher order moments is less clear. Naively, the Kaiser analysis would seem to indicate that the J-point hierarchical redshift amplitudes S_J^z should be smaller than the real amplitudes S_J, by a factor $S_J^z/S_J \sim [1 + f(\Omega)/3]^{1-J}$, and therefore be sensitive to Ω. However, extending the analysis to second order perturbation theory, required to compute the 3-point function consistently, Bouchet *et al.* (1992) claim that the net effect of redshift distortions on S_3 is small. Numerically, Lahav *et al.* (1993) find in simulations on smaller scales that S_3 is quite distorted in redshift space, while Coles *et al.* (1993) do not. Further complicating the theoretical expectations is the possibility of biasing, i.e. whether or not galaxies faithfully trace the matter distribution. For large scales, Fry and Gaztañaga (1993) have shown that a local biasing preserves the hierarchical structure to all orders but can change the values of the S_J. Kaiser's effect, arising from the peculiar velocity modulation of the distribution, applies equally to the galaxy number distribution, even when galaxies are not unbiased tracers of the mass, and in general all these effects are mixed at each order.

To separate redshift distortions of observed correlations from other sources of difference, we believe that it is important to perform a dual analysis to the same data samples. Thus, in this paper we present an analysis in which identical techniques of estimation are applied over the same data samples to compute volume average correlations in redshift space for volumes that are expected to exhibit redshift distortions, and for configurations that are expected to minimal distortions. In § 2 we discuss measuring correlations from moments of counts in cells, including an analytic extension of the count-in-cell tails for finite volume samples. In § 3, we relate volume average parameters to intrinsic parameters for spherical and conical cells for power-law underlying correlations. Spherical cells are expected to experience redshift distortions, which should be minimal in conical cells. § 4 presents details of the samples we use and the data analysis. § 5 contains a summary of results and a final discussion.

2 Estimation of volume-average correlations

We center our analysis on the the volume-average correlation functions,

$$\bar{\xi}_J(V) = \frac{1}{V^J} \int_V d^3r_1 \ldots d^3r_J \, \xi_J(\boldsymbol{r}_1, \ldots, \boldsymbol{r}_J). \tag{1}$$

We use volume-limited samples so that no selection function appears. We assume that every region in redshift space is equally weighted and faithfully traced by the galaxies in each sample.

We use the count-in-cell probabilities $P_n(V)$ to compute moments and obtain the $\bar{\xi}_J(V)$. The correlation functions $\bar{\xi}_J(V)$ can be found from the count-in-cell probabilities $P_n(V)$, the probability to find n galaxies in a randomly selected cell of volume V, from moments $\langle(\Delta n)^J\rangle$. Including discreteness contributions (cf. Peebles 1980; Fry 1985), the first few moments are related to the $\bar{\xi}_J(V)$ as

$$\begin{aligned}
\langle n \rangle &= \bar{N} \\
\langle (\Delta n)^2 \rangle &= \bar{N}^2\bar{\xi}_2 + \bar{N} \\
\langle (\Delta n)^3 \rangle &= \bar{N}^3\bar{\xi}_3 + 3\bar{N}^2\bar{\xi}_2 + \bar{N} \\
\langle (\Delta n)^4 \rangle - 3\langle (\Delta n)^2 \rangle^2 &= \bar{N}^4\bar{\xi}_4 + 6\bar{N}^3\bar{\xi}_3 + 7\bar{N}^2\bar{\xi}_2 + \bar{N}
\end{aligned} \tag{2}$$

2.1 Count-in-cell probabilities

We estimate $P_n(V)$ in the following way: given the radius of a test-sphere, we choose randomly a center inside the survey sample, count the number of galaxies found inside the cell, and accumulate the number of cells N_n with $n = 0, 1, 2, 3\ldots$ galaxies. We repeat this procedure N_T times, to be chosen so that the sampling spheres will overlap with each other. Counts-in-cell probabilities are then estimated by $P_n = N_n/N_T$. The precision of this estimation is limited by the number of *independent* cells; from the Poisson distribution, we expect $\Delta P_n/P_n \gtrsim (P_n N_T)^{-1/2}$ for $P_n \ll 1$. We have to choose N_T in order to estimate counts in cells with the right accuracy. A better choice is $N_T = \bar{\xi}_2^{-3/2} V_T/V$ (Gaztañaga & Yokoyama 1993), but because $\bar{\xi}_2$ is not known a priori we must iterate the process to obtain N_T, using as a first approximation the value of $\bar{\xi}_2$ estimated from pair-counts. The results do not differ much between these two prescriptions, and therefore we have chosen the one that is more simple, i.e. $N_T = 2V_T/V$. Error bars for the P_n are estimated from 90% confidence in different realizations of the positions of the independent cells, which agree well with the binomial estimate of errors above.

2.2 Estimation of moments

Once we have the $P_n(V)$, we next calculate moments of different orders to estimate the correlation functions from equation (2). This brings us to the finite sample problem. The number of independent cells N_T used to estimate $P_n(V)$ is necessarily finite, because the size of the sample is finite. This limits the smallest value of P_n that can be estimated, $P_{\rm min}(V_c) \sim 1/N_T$. There will also be a maximum cell count, $n_{\rm max}$. The probabilities P_n for counts $n > n_{\rm max}$ and with $P_n < P_{\rm min}$ can not be estimated, and thus the moments, nominally given by

$$\langle n^m \rangle = \sum_{n=0}^{\infty} n^m P_n\,, \tag{3}$$

can only be summed up to $n = n_{\rm max}$. An estimate of when this is an important effect is whether $n_{\rm max}$ is small relative to $N_c = \bar{N}\bar{\xi}_2$, the number of galaxies in a "typical" cluster.

If $n_{\max} < N_c$, then the moments will be systematically underestimated, by an increasing amount for higher moments. When only a few rich clusters such as Virgo or Coma are present in a catalog (such as the CfA) there may also be a "bump" in the tail of P_n. This "bump" may introduce a large artificial enhancement of the correlation functions. A further related problem is interaction with the boundary: when cell locations are restricted to avoid intersection with the boundaries, the size of the survey area covered gets smaller as the size of the cell is increased. This can introduce additional bias, as the center area of the sample is more weighted than the boundary, and, moreover, reduces even further the number of independent cells, so that $P_{\min}$ is larger and $n_{\max}$ is smaller, which again eventually results in underestimated moments. When the sample is large enough that finite sample size is not a problem, the P_n appear to fall exponentially with n. This suggests a method to correct for the limitations of finite volume.

Modeling the tail, that is, extrapolating the P_n to $n > n_{\max}$, can help to compensate for the underestimation, or, at the least, can be used to study systematic errors in the moments. Both observations and various scale-invariant models suggest that the probability tails are exponential, behaving as $P_n \propto e^{-n/N_c}$, where $N_c = \bar{N}\bar{\xi}_2$. Thus, when $n_{\max} > N_c$, the contribution to $\sum n^m P_n$ from $n_{\max}$ to ∞ is small when compared with the whole sum in equation (3), as claimed above. Modeling also reduces the effects on the correlations that appears when rich clusters such as Coma are present. By fitting an exponential to the tail, the effect of a "bump" in the P_n is diluted.

We fit the tail of the observed counts-in-cells to an exponential function, $\langle N_n \rangle = \mu_n = Ce^{-\alpha n}$, using a Poisson likelihood function,

$$\mathcal{L} = \sum_n \log\left[\frac{1}{N_n!}\mu_n^{N_n} e^{-\mu_n}\right], \tag{4}$$

where N_n are the observed counts (the number of cells with n galaxies) and $\mu_n = Ce^{-\alpha n}$. The values of C and α are found by maximization of the likelihood $\mathcal{L}$. As a test we can verify that the observed counts in the tail follow a Poisson distribution around the exponential. In practice we construct a routine to find the value n_1 where the "tail" begins, i.e. the value of i where the counts begin to fit an exponential (ideally, $\bar{N} \ll n_1 \ll n_{\max}$), fit $\mu_n = Ce^{-\alpha n}$ for $n_1 < n < n_{\max}$, and extrapolate $P_n \sim \mu_n$ for $n > n_{\max}$. We then must renormalize the distribution of counts so that $\sum_0^\infty \bar{P}_n = 1$. For small cell volume, the resulting correction to the moments is very small, as $n_{\max}$ is already quite large, while for large cells, both the contribution from and the uncertainties in this modeling could be very large. To estimate the systematic errors introduced in the moments by modeling the exponential tail, we report in the results the difference between the "raw" moments (without modeling of the tails) and the modeled moments,

$$\Delta\langle n^m \rangle = \left| \sum_{n=0}^{\infty} n^m \bar{P}_n - \sum_{n=0}^{n_{\max}} n^m P_n \right| . \qquad (5)$$

This provides a natural way to measure when the finite volume effects are large.

3 Volume average correlations

3.1 Redshift vs. real space correlations

The choice of volume shape can emphasize or minimize the effects of peculiar velocities. As one choice, we compute moments over spheres of radius R in redshift space. As remarked above, the contribution of peculiar velocities to the apparent redshift distance are expected to distort the resulting statistics. We refer to the results from spherical volumes as "redshift" results. To extract information about correlations from a redshift catalog that is not distorted by the peculiar velocity modulation of the distribution, we simply change the shape of the volume, to cells with the shape of conic sectors of a sphere between radii $d < r < D$, of opening angle θ around a radial axis (in our analysis, d is a fixed to $2500\,\mathrm{km\,s^{-1}}$ and D is the depth of the sample; see Table 1). The estimated counts-in-cells for these volumes are not distorted except perhaps at the inner and outer radial boundaries of the cell, where peculiar velocities can move a few galaxies in or out of the cell, a small effect for deep samples. Because results from these conic volumes are not distorted by peculiar velocities, we refer to them in brief as "real space" results. As will become apparent below, the conic cell analysis is similar to considering just the projected, magnitude-limited angular distribution, with integrals similar to those in the standard angular analysis. However, since redshift information is used to determine the distance and absolute magnitudes of the galaxies in our samples, the resulting analog of the Limber equation (see Peebles 1980) for these volume-limited samples does not involve an integral over the luminosity function, thus removing a source of uncertainty.

3.2 Power-law correlations

In extracting the underlying correlation functions from the volume-averaged results, we assume a power-law two-point correlation function, $\xi_2(r) = (r_0/r)^\gamma$, and a hierarchical three-point function, as suggested by our data (see Figs. 1a–c). The power law model $\xi_2(r) = (r_0/r)^\gamma$ is not a good approximation for all possible ranges of scales (see i.e. Groth & Peebles 1977; Maddox *et al.* 1990) but, given the resolution in our analysis, it is quite a good one for the range of scales we have been able to inspect; i.e. $R \simeq 1$–$20\,h^{-1}\,\mathrm{Mpc}$.

The volume-average two-point correlation is

$$\bar{\xi}_2(V) = \frac{1}{V^2}\int_V d^3r_1 d^3r_2\, \xi_2(|\boldsymbol{r}_1 - \boldsymbol{r}_2|). \tag{6}$$

For $\xi_2(r) = (r_0/r)^\gamma$ and spherical cells of radius R, we have

$$\begin{aligned} \bar{\xi}_2^S &= S(\gamma)\,(r_0/R)^\gamma \\ S(\gamma) &= \frac{2^{-\gamma}}{(1-\gamma/3)(1-\gamma/4)(1-\gamma/6)}, \end{aligned} \tag{7}$$

so that $\bar{\xi}_2^S(R)$ is also a power law, with, in the absence of peculiar velocity distortions, the same slope as $\xi_2(r)$ and with amplitude different by a factor $S(\gamma)$ of order unity. For $\gamma = 2$, $S(\gamma) = 9/4$; for $\gamma = 1.5$, $S \approx 1.5$.

For a volume shaped as conic sector of an sphere of opening angle θ around a radial axis between radii $d < r < D$ we find for power-law $\xi_2(r)$ in the limit $\theta \ll 1$,

$$\begin{aligned} \bar{\xi}_2^C &= C(\gamma)\,\theta^{1-\gamma} \\ C(\gamma) &= \frac{I_1}{I_0^2}\frac{H_\gamma}{2\pi}\left(\frac{r_0}{D}\right)^\gamma \\ H_\gamma &= \int_{-\infty}^{\infty}\frac{dx}{(1+x^2)^{\gamma/2}} = \frac{\Gamma(1/2)\,\Gamma(\gamma/2-1/2)}{\Gamma(\gamma/2)} \\ I_k &= \frac{1-(d/D)^{3(k+1)-k\gamma}}{3(k+1)-k\gamma}\int_0^1 z\,dz\,F^k(z) \\ F(z) &= \int_0^1 x\,dx\int_0^{2\pi} d\phi\,(z^2+x^2-2zx\cos\phi)^{(1-\gamma)/2} \end{aligned} \tag{8}$$

so that $\bar{\xi}_2^C$ is also a power law but with a different slope and (possibly greatly) reduced amplitude, $\bar{\xi}_2^C(\theta) \sim \xi(D)\,\theta^{1-\gamma}$. In each case, from the fitted slope and amplitude of observed $\bar{\xi}_2$ and from the expressions above, one can estimate the values of r_0 and γ for the intrinsic two-point correlation function.

For higher order correlations we assume hierarchical properties, $\bar{\xi}_J = S_J\bar{\xi}_2^{J-1}$, again in agreement with our data (see Figs. 2–3) and previous analyses. For the 3-point correlation function we use the local hierarchical expression

$$\xi_3(\boldsymbol{r}_1,\boldsymbol{r}_2,\boldsymbol{r}_3) = Q_3\,\left[\xi_2(r_{12})\xi_2(r_{13}) + \xi_2(r_{12})\xi_2(r_{23}) + \xi_2(r_{13})\xi_2(r_{23})\right] \tag{9}$$

to compute the volume average

$$\bar{\xi}_3(V) = \frac{1}{V^3}\int_V d^3r_1 d^3r_2 d^3r_3\, \xi_3(\boldsymbol{r}_1,\boldsymbol{r}_2,\boldsymbol{r}_3). \tag{10}$$

We are interested in the hierarchical amplitudes, i.e. we want to estimate: $S_3 = \bar{\xi}_3(V)/\bar{\xi}_2^{/,2}(V)$. For a spherical volume, the hierarchical relation (9) with $\xi_2(r) = (r_0/r)^\gamma$ implies:

$$S_3^S = 3\,\eta(\gamma)\,Q_3$$

$$\eta(\gamma) = \frac{(6-\gamma)^2}{3(2-\gamma)^2}\left[\frac{46-48\gamma+17\gamma^2-2\gamma^3}{2(7-2\gamma)(9-2\gamma)} - \frac{2^{2\gamma}\sqrt{\pi}\,(2-\gamma)\Gamma(5-\gamma)}{256\,\Gamma(9/2-\gamma)} - \frac{2^{2\gamma}\sqrt{\pi}\,\Gamma(5-\gamma)}{256\,\Gamma(11/2-\gamma)}\right] \tag{11}$$

(Gaztañaga & Yokoyama 1993). For $0 \leq \gamma \leq 2$, S_3 and $3Q_3$ differ by less than 3%, so that in practice one can use as a good approximation $S_3^S \simeq 3Q_3$. In our analysis, averages over spherical volumes and thus S_3^S are obtained in redshift space.

For the conic cell shape we have, in the limit of small θ,

$$S_N^C = N^{N-2} Q_N \frac{I_0^{N-2}\, I_{N-1}}{I_1^{N-1}} \tag{12}$$

where I_N is defined in equation (8) above. Thus, by measuring S_3^C and γ for conic cells one can use the above relations to estimate the corresponding Q_3 or S_3^S in real space.

4 Data analysis results

4.1 Catalogues

We use three different catalogs of galaxies:

- *i*) the North Zwicky Center for Astrophysics catalog (Huchra *et al.* 1983, hereafter CfA), with $m_B < 14.5$, $\delta \geq 0$, and $b^{\rm II} \geq 40°$, which has a solid angle of 1.83 sr.

- *ii*) the Southern Sky Redshift Survey (Da Costa *et al.* 1991, hereafter SSRS) of diameter-selected galaxies with $\log d(0) \geq 0.1$ from the ESO catalog with $\delta \leq -17.5°$, $b^{\rm II} \leq -30°$; the solid angle is 1.75 sr.

- *iii*) the full-sky coverage redshift survey of galaxies from the IRAS(*Infrared Astronomical Satellite*) database (Strauss *et al.* 1992, hereafter IRAS) with limiting flux density of 1.936 Jy at 60 μm and galactic latitude $|b| > 5°$; the solid angle is 11.0 sr.

We select four different volume-limited subsamples from each catalog, as shown in Tables 1–3, where $z_{\rm lim}$ is the maximum redshift, $N_{\rm tot}$ is the total number of galaxies, V_T is the volume of each sample, and M_B, $d_{\rm lim}$, and $z^2 f_{60}$ are the limiting absolute magnitude, "face-on" diameter, and flux, respectively. Lengths in the tables quoted as "Mpc" use $H_0 = 100$. To produce fair volume-limited samples we have not included the fainter or smaller galaxies, so that the space in each sample is homogeneously filled. For example, each CfA sample includes galaxies brighter than $M_B = m_B - 25 - 5\log(z_{\rm lim}/H_0)$, where $m_B = 14.5$ is the limiting apparent magnitude. In addition, galaxies in the CfAN50 sample are restricted to be fainter than $M_B = -20.3$, so that this sample is independent of CfAN90. In the SSRS catalogue, each sample includes galaxies with physical diameter greater than $d_{\rm lim} = z_{\rm lim}\theta_{\rm cut}/H_0$,where $\theta_{\rm cut} = 1'.26$ is the "face-on" diameter cut-off. In the IRAS catalogue, each sample includes galaxies with absolute flux $z^2 f_{60}$ greater than the limiting flux $z_{\rm lim}^2\,1.936\,{\rm Jy}$.

Heliocentric redshifts are corrected only for our motion with respect to the rest frame of the Cosmic Microwave Background; $v = 365\,{\rm km\,s^{-1}}$ toward $(\alpha, \delta) = (11.2^{\rm h}, -7^\circ)$ (Smoot *et al.* 1991). Galaxies with redshifts smaller than $2500\,{\rm km\,s^{-1}}$ are excluded, since at these scales typical peculiar velocity flows (of several hundreds of km/s) can compete with the general recession velocity.

4.2 Count-in-cell volumes

For each sample, we want to estimate the count-in-cell probabilities P_n as a function of the cell volume. The total number of degrees of freedom is limited by the density $\bar{n}$ of the sample and its total volume V_T, so that the size of the cell is bounded bellow by $\bar{n}$ and above by V_T. The number of different cell sizes and their intervals should not be set arbitrarily, as the resulting moments or correlations at each point would not be independent. For samples of small density, a good criterion for statistically independent sizes is $V_i = i/\bar{n}$, for $i = 1, 2, \ldots$, as then each new volume includes on average one more galaxy. Notice how different this is from using equal spacing in the radius of spherical cells for all samples; this not only introduces a different weighting but also imposes an arbitrary number of degrees of freedom, regardless of the size or density of the sample. In our analysis we use equal volume spacing in units of $V_1 = 1/\bar{n}$. We use half this unit to study the fluctuations or when we have only few points. The largest cell to be used is limited by the boundaries of the sample. Using different boundary conditions, Gaztañaga (1992) and Gaztañaga & Yokoyama (1993) have found that a good phenomenological bound is $V \leq V_T/3^3$, so that the diameter of the cell is at most one third of the typical size of the sample. This is just one upper limit; we also discard the larger cells of our analysis when the estimated uncertainties, from equation (5) are too large. The resulting range of scales displayed in Tables 4–6 is different for each sample. The larger samples can accommodate larger cells, but also have smaller densities and thus do not have information on the smaller scales.

4.3 Correlation functions

We estimate the correlation functions using the moments of counts-in-cells as explained in section § 2. Figures 1*a*–*c* show the volume average two-point correlation function, $\bar{\xi}_2$, as a function of the size of the cell. Open squares correspond to spherical ("redshift") cells and triangles correspond to conic ("real space") cells. The scale of the cell, given in Mpc with $H_0 = 100$, corresponds to the radius R of the redshift-space sphere or the radius of the base of the conical sector, θD with D the depth of the sample. The error of each point is the maximum between the systematic error (5) from correcting the count distribution tail for finite volume and the statistical error from the P_n propagated to the moments. The dashed line in each figure is the best fit to a power law, weighted by the errors. The agreement with a power law model justifies our assumption of the relations in section § 3. The slopes for the conic cells (triangles) and spherical shells (squares) follow what we expect from the projection, $\bar{\xi}_2^C \sim \theta^{1-\gamma} D^{-\gamma}$ and $\bar{\xi}_2^S \sim R^{-\gamma}$. In Tables 4–6 we display the values of the fit in terms of the slope γ and correlation length r_0 of the intrinsic correlation function $\xi_2(r) = (r_0/r)^\gamma$ using equation (7) and equation (8). Note that the range of scales where the fit is done is different for each sample, as explained above. We quote both the statistic and the systematic error (the last in parenthesis). The errors in the fitted parameters, r_0 and γ, reflect both the goodness of the fit and the statistic (or systematic) error in the estimated correlations; both contributions are usually of comparable magnitude.

Figures 2*a*–*c* show $\bar{\xi}_3(R)$ (triangles) and $\bar{\xi}_4(R)$ (squares) for spherical (redshift) cells, plotted against $\bar{\xi}_2(R)$ for all samples. In Figures 3*a*–*c* we present a similar plot for conical (real space) cells. Again, the error plotted at each point is the maximum between the systematic error (eq. [5]) and the statistical error from the P_n propagated to the moments. The dashed line is the best fit to $\bar{\xi}_3 = S_3 \bar{\xi}_2^2$ and $\bar{\xi}_4 = S_4 \bar{\xi}_2^3$ weighted by the errors. The agreement of these power law models is evidence in favor of the hierarchical model and, again, justifies our assumptions in section § 3.

Tables 4–6 shows the parameters S_3 and S_4 of the fit. The values of S_3 for conical cells have been scaled to the corresponding value of a spherical cell using equation (11) and equation (12), so that real space and redshift space amplitudes can be directly compared. The correction to convert S_3^C into S_3^S is smaller than 15% so that we have not propagated the uncertainties from γ in this conversion. Because this correction turns out to be small and there are large uncertainties in S_4 we have not tried to calculate the exact correction in the case of the 4-point function, but have just scaled the correction found for S_3 using the dimensional argument $S_4^S/S_4^C \simeq [S_3^S/S_3^C]^2$. We quote both the statistic and the systematic error (the last in parenthesis). The errors in the fitted parameters S_3 and S_4 reflect both the goodness of the fit and the statistic (systematic) error in the estimated correlations; both contributions are usually of comparable magnitude. Samples IRAS65 and IRAS80 have a very noisy signal for spherical cells and results are not quoted.

The average values reported in Tables 4–6 are the mean values for all samples within a catalog, weighted by $1/\sigma_i^2$ (using the maximum between the statistic and systematic errors).

The first error in the average is the weighted dispersion about the mean, scaled to a 1-σ interval after accounting for the difference between the Gaussian and Student-t distribution. For most averages, with four degrees of freedom, the dispersion is increased by the factor 1.14163. In parentheses we also quote the expected error, $1/\sum(1/\sigma_i^2)$. These two are the same when (reduced) $\chi^2 = 1$.

4.4 Redshift distortions

In the linear regime Kaiser (1987) has derived the expected ratio of two-point function in redshift space, $\xi_2(s)$, to that in real space, $\xi_2(r)$:

$$\frac{\xi_2(s)}{\xi_2(r)} = 1 + \frac{2}{3}\frac{\Omega^{4/7}}{b} + \frac{1}{5}\frac{\Omega^{8/7}}{b^2}, \tag{13}$$

where b is the bias factor between matter fluctuations and galaxy fluctuations, $\delta_g = b\delta_m$. Lilje & Efstathiou (1989) have shown that these redshift distortions are expected even on mildly non-linear scales where $\xi_2(r) \sim 1$. Non-linear effects and the "fingers of God" for smaller scales tend to suppress the redshift correlations, so that $\xi_2(s)/\xi_2(r)$ becomes smaller than 1 for small separations (Davis & Peebles 1983). Therefore, even if we have not reached the scales where the linear theory should apply (whatever this scale is), we should be able to place a lower bound on $\Omega^{4/7}/b$ from the maximum redshift distortion we are able to detect.

As will become apparent, we can not use our data to make an accurate determination of this effect, but we can estimate the order of magnitude. At some point the power laws we have observed for the real and redshift two-point correlations will break to reproduce Kaiser's results, a constant ratio of $\xi_2(s)$ to $\xi_2(r)$. The ratio we see on larger scales is not constant, but rising with scale, except in one case. Even though in our analysis this ration has not reached a constant value, presumably because of poor sensitivity at large scales, we can use the extra power observed in the redshift correlation to place a lower bound on the factor $\Omega^{4/7}/b$, and, if $\Omega = 1$, an upper bound on b. Using the values of r_0, s_0 and γ shown in Tables 4–6, we estimate the ratio $\xi_2(s)/\xi_2(r)$ at r_0 and at the scale r_{max} corresponding to the largest spherical (redshift) cell in each sample. Table 7 shows r_{max}, the value of the intrinsic two-point (real-space) correlation, the correlation strength at that scale, $\xi_2(r_{\mathrm{max}})$, and the resulting values of $\Omega^{4/7}/b$ resulting from equation (13). As argued above, the ratio $\xi_2(s)/\xi_2(r)$ increases towards larger scales, and thus the final column represents our strongest lower bound on $\Omega^{4/7}/b$. Errors in $\Omega^{4/7}/b$ are propagated from the errors in r_0, s_0, and γ (again, the maximum between the statistic and systematic errors). The average values in Table 7 are the mean values for all samples within a catalog, weighted by the errors. The negative values of $\Omega^{4/7}/b$ for CfAN65 do not affect the average value much, but do increase the estimated dispersion by a factor of 2.

5 Discussion

In this work, we have computed volume-averaged correlation functions $\bar{\xi}_2$, $\bar{\xi}_3$ and $\bar{\xi}_4$ for conical and spherical configurations that allow us to observe the effects of peculiar velocity distortions. We have considered volume-limited samples so that no assumption has to be made about a luminosity function. We make use all the degrees of freedom in each sample and weight them properly. To account for boundary and finite size effects we have introduced a modeling of the tail of the distribution of fluctuations which helps to improve the signal and estimate the uncertainties. We report the difference between results obtained with and without this modeling of the tail as a systematic error, which we have taken as the minimum uncertainty in our results, a conservative approach that leaves our conclusions safely unaffected by our assumptions. To simplify comparisons of the analyses of different samples we have reduced the observed correlation functions, $\bar{\xi}_2(R)$, $\bar{\xi}_3(R)$, and $\bar{\xi}_4(R)$ in Figures 1–3, to a few parameters shown in Tables 4–6.

Our analysis reproduces the already known trend (Davis *et al.* 1988) that the amplitude s_0 of the two-point redshift correlation function of optical galaxies grows with the depth of the survey, at least up to a redshift of $8000\,\mathrm{km\,s^{-1}}$. This trend is confirmed here for both the Southern and Northern galactic hemispheres for optical selected galaxies, i.e. in both the SSRS and CfA catalogs; within our poor resolution, it is not observed in the IRAS samples. As a new result, we find that this scaling with depth seems to occur also in real space, which indicates that it can not just be a consequence of redshift distortions. We also find that for depths larger than $8000\,\mathrm{km\,s^{-1}}$ the trend is broken: the observed correlation length decreases in the $9000\,\mathrm{km\,s^{-1}}$ samples. This indicates that the effect may be accidental or caused by sampling an "unfair" local volume, but does not imply a simple "fractal" or inhomogeneous behavior.

For the average values and even for separate subsamples within each catalog, the intrinsic 2-point correlation length r_0 of the CfA and SSRS are very similar. The relative amplitude of the IRAS and CfA two-point correlations is in very good agreement with other analyses (Strauss *et al.* 1992; Saunders, Rowan-Robinson, & Lawrence 1992) although the techniques and samples used are quite different. There is a significant difference between the average slope γ of $\xi_2 \sim r^{-\gamma}$ in real space between the SSRS and the CfA or IRAS catalogues. The slope in the SSRS, $\gamma = 1.62 \pm 0.04$, is lower than the "standard" value of $\gamma = 1.8$, but the errors are quite large. SSRS diameter magnitudes are more subject to plate-to-plate correction which might introduce some large scale power. There is also a very large void in this catalog (larger than any in the CfA1).

In general, there is a characteristic redshift distortion on $\xi_2(r)$: the slope γ is flatter and the correlation length is larger in redshift space than in real space, that is, redshift distortions "move" correlations from small to large scales. In particular, for the average values, going from real to redshift space reduces the slope of $\bar{\xi}_2$ by 30% (SSRS), 20% (IRAS) and 13% (CfA). At the largest scales the extra power in the redshift distribution is compatible with a $\Omega^{4/7}/b \simeq 1$, as seen in Table 7. As expected, the average values of $\Omega^{4/7}/b$ for each catalog are correlated with the amount of reduction in the redshift slope. Our results for $\Omega^{4/7}/b$ in the CfA are much larger than those deduced by Lilje & Efstathiou (1989) from Figure 3 of Davis & Peebles (1983), perhaps because they only use scales up to $7\,h^{-1}$ Mpc, whereas ours reach to $12\,h^{-1}$ Mpc.

The higher order correlations $\bar{\xi}_3$ and $\bar{\xi}_4$ are redshift distorted also, but in such a way that the hierarchical amplitudes S_3 and S_4 are insensitive to these distortions, within the resolution of our analysis. This is in agreement with the numerical studies of Coles *et al.* (1993). It follows that redshift distortions are probably not responsible for the discrepancies in the values of S_3 and S_4 found in some of the previous analyses, summarized in Table 8. Moreover, the hierarchical amplitudes S_3 and S_4 are constant as a function of scale between 1–20 h^{-1} Mpc (which includes the transition between linear and non-linear scales), and they have a similar value in all samples, even for different catalogues, despite that $\bar{\xi}_2$, $\bar{\xi}_3$ and $\bar{\xi}_4$ differ from one sample to another by large factors (up to factors of 4 in $\bar{\xi}_2$, or 8 for $\bar{\xi}_3$, or 12 for $\bar{\xi}_4$). This is remarkable given the different criteria in the selection of galaxies and also the difference in the resulting range of densities, luminosities and locations between samples.

Acknowledgements

After this work was completed we became aware of other work on exponential modeling of the probability tail by Colombi, Bouchet, & Schaeffer (1993), who also test their prescription with numerical simulations. E. G. acknowledges useful discussions with Jun'ichi Yokoyama. This work was supported in part by DOE and by NASA (grant NAGW-2381) at Fermilab.

References

Bouchet, F. R., Davis, M., & Strauss M. 1993, in *Proceedings DAEC Workshop*, ed. G. Mamon, in press

Bouchet, F. R., Juszkiewicz, R., Colombi, S., & Pellat, R., 1992, ApJ, 394, L5

Coles, P., Moscardini, L., Lucchin, F., Matarrese, S., & Messina, A. 1993, preprint

Colombi, S., Bouchet, F. R., & Schaeffer, R. 1993, A&A (in press)

Da Costa, L. N., Pellegrini, P., Davis, M., Meiksin, A., Sargent, W., & Tonry, J. 1991, ApJ Suppl, 75, 935

Davis, M., & Peebles, P. J. E. 1983, ApJ, 267, 465

Davis, M., Meiksin, A., Strauss, M. A., da Costa, L. N., & Yahil, A. 1988, ApJ, 333, L9

Fry, J. N. and Peebles, P. J. E. 1978, ApJ, 221, 19

Fry, J. N. 1985, ApJ, 289, 10

Fry, J. N., & Gaztañaga, E. 1993, ApJ (in press) (FERMILAB-Pub-92/367-A)

Gaztañaga, E. 1992, ApJ, 398, L17

Gaztañaga, E., & Yokoyama, J 1993, ApJ, 403, 450

Groth, E. J., & Peebles, P. J. E. 1977, ApJ, 217, 385

Huchra, J., Davis, M., Latham, D., & Tonry, J. 1983, ApJSuppl, 52, 89

Lahav, O., Itoh, M, Inagaki, S., & Suto Y. 1993, ApJ, 402, 387

Lilje, P. B., & Efstathiou, G. 1989, MNRAS, 236, 851

Kaiser, N. 1987, MNRAS, 227, 1

Maddox, S. J., Efstathiou, G., Sutherland, W.J. & Loveday, L. 1990, MNRAS, 242, 43p

Meiksin, A., Szapudi, I. & Szalay, A. S. 1992, ApJ, 394, 87

Peebles, P. J. E. 1980, *The Large-Scale Structure of the Universe* (Princeton: Princeton Univ. Press)

Saunders, W., Rowan-Robinson M., & Lawrence A. 1992, MNRAS, 258, 134

Strauss, M. A., Davis, M., Yahil, A. & Huchra, J. P. 1992, ApJ, 385, 421

Strauss, M. A., Huchra, J. P, Davis, M., Yahil, A., Fisher, K., &Tonry, J. 1992, ApJSuppl., 83, 29

Smoot, G. F. *et al.* 1991, ApJ, 371, L1

Szapudi, I., Szalay, A. S., & Boschan, P. 1992, ApJ, 390, 350

TABLE 1
CfA Samples

Sample	$z_{\rm lim}$ (km/s)	M_B	$N_{\rm gal}$	V_T (Mpc^3)
CfAN50	5000	$[-20.3, -19.0]$	206	6.7×10^4
CfAN65	6500	< -19.5	208	1.6×10^5
CfAN80	8000	< -20	207	3.0×10^5
CfAN90	9000	< -20.3	146	4.4×10^5

TABLE 2
SSRS Samples

Sample	$z_{\rm lim}$ (km/s)	$d_{\rm lim}$ (kpc)	$N_{\rm gal}$	V_T (Mpc^3)
SSRS50	5000	18.3–33	222	6.7×10^4
SSRS65	6500	> 22	283	1.5×10^5
SSRS80	8000	> 29.3	220	2.9×10^5
SSRS90	9000	> 33	203	4.2×10^5

TABLE 3
IRAS Samples

Sample	$z_{\rm lim}$ (km/s)	$z^2 f_{60}$ (Jy Mpc^2)	$N_{\rm gal}$	V_T (Mpc^3)
IRAS45	4500	> 3920	319	3.3×10^5
IRAS55	5500	> 5856	404	6.1×10^5
IRAS65	6500	> 8180	359	1.0×10^6
IRAS80	8000	> 12390	314	1.9×10^6

TABLE 4*a*

CfA Results, Real Space

Sample	$\theta z_{\rm lim}$ (Mpc)	γ	r_0 (Mpc)	S_3	S_4
CfAN50....	1–6	1.88 ± 0.03 (0.05)	3.68 ± 0.11 (0.21)	1.98 ± 0.22 (0.70)	6.0 ± 3.6 (4.1)
CfAN65....	1–8	1.82 ± 0.02 (0.04)	4.98 ± 0.10 (0.17)	1.87 ± 0.13 (0.52)	5.6 ± 4.8 (3.1)
CfAN80....	2–10	1.76 ± 0.05 (0.09)	7.09 ± 0.53 (0.88)	1.91 ± 0.18 (0.50)	5.4 ± 2.2 (1.3)
CfAN90....	3–14	2.26 ± 0.13 (0.12)	5.75 ± 0.70 (0.64)	2.03 ± 0.45 (0.43)	9.8 ± 3.7 (3.9)
Average....	1–14	1.86 ± 0.07 (0.03)	4.56 ± 0.50 (0.13)	1.95 ± 0.04 (0.26)	6.3 ± 1.1 (1.6)

TABLE 4*b*

CfA Results, Redshift Space

Sample	R (Mpc)	γ	s_0 (Mpc)	S_3	S_4
CfAN50....	2–7	1.62 ± 0.08 (0.10)	4.47 ± 0.27 (0.33)	1.77 ± 0.13 (0.33)	4.9 ± 0.9 (1.7)
CfAN65....	3–8	1.89 ± 0.23 (0.36)	4.81 ± 0.86 (1.33)	1.57 ± 0.16 (0.53)	2.9 ± 1.0 (2.7)
CfAN80....	4–13	1.56 ± 0.06 (0.10)	8.13 ± 0.64 (1.06)	2.34 ± 0.14 (0.62)	7.8 ± 1.0 (3.5)
CfAN90....	8–16	1.82 ± 0.22 (0.45)	6.83 ± 1.61 (3.31)	2.57 ± 0.29 (0.85)	10.2 ± 2.4 (6.1)
Average....	2–16	1.61 ± 0.05 (0.07)	4.81 ± 0.67 (0.31)	1.88 ± 0.31 (0.24)	5.1 ± 1.2 (1.3)

TABLE 5*a*

SSRS Results, Real Space

Sample	$\theta z_{\rm lim}$ (Mpc)	γ	r_0 (Mpc)	S_3	S_4
SSRS50....	1–6	1.64 ± 0.02 (0.03)	3.60 ± 0.33 (0.45)	1.72 ± 0.14 (0.30)	4.8 ± 4.7 (1.6)
SSRS65....	1–8	1.57 ± 0.01 (0.03)	5.27 ± 0.14 (0.47)	2.09 ± 0.15 (0.82)	6.2 ± 4.6 (4.4)
SSRS80....	2–7	1.64 ± 0.09 (0.10)	5.69 ± 0.57 (0.69)	1.77 ± 0.18 (0.23)	5.0 ± 3.6 (1.8)
SSRS90....	2–12	1.71 ± 0.04 (0.06)	4.80 ± 0.24 (0.36)	1.78 ± 0.48 (0.93)	6.3 ± 2.3 (5.7)
Average....	1–12	1.62 ± 0.03 (0.02)	4.70 ± 0.46 (0.23)	1.77 ± 0.05 (0.17)	5.4 ± 0.4 (2.2)

TABLE 5*b*

SSRS Results, Redshift Space

Sample	R (Mpc)	γ	s_0 (Mpc)	S_3	S_4
SSRS50....	2–6	1.32 ± 0.08 (0.11)	4.79 ± 0.35 (0.51)	1.65 ± 0.10 (0.33)	4.0 ± 0.5 (1.8)
SSRS65....	3–9	1.05 ± 0.02 (0.05)	9.16 ± 0.32 (0.77)	1.97 ± 0.06 (0.48)	5.5 ± 0.4 (2.2)
SSRS80....	4–10	1.30 ± 0.11 (0.13)	9.15 ± 1.41 (1.71)	1.97 ± 0.11 (0.35)	5.6 ± 0.8 (1.7)
SSRS90....	5–11	1.25 ± 0.22 (0.25)	8.15 ± 2.49 (2.85)	1.83 ± 0.17 (0.37)	5.3 ± 1.4 (2.2)
Average....	2–11	1.12 ± 0.08 (0.04)	6.33 ± 1.36 (0.41)	1.83 ± 0.09 (0.19)	5.1 ± 0.5 (1.0)

TABLE 6*a*

IRAS Results, Real Space

Sample	$\theta z_{\rm lim}$ (Mpc)	γ	r_0 (Mpc)	S_3	S_4
IRAS45....	2–13	1.89 ± 0.02 (0.04)	3.85 ± 0.15 (0.27)	2.06 ± 0.25 (0.38)	7.4 ± 6.1 (2.9)
IRAS55....	2–17	1.75 ± 0.02 (0.03)	4.04 ± 0.10 (0.18)	2.44 ± 0.52 (0.48)	9.4 ± 5.9 (4.0)
IRAS65....	3–20	1.76 ± 0.11 (0.15)	3.80 ± 0.44 (0.60)	2.33 ± 1.35 (0.69)	11.7 ± 9.6 (9.2)
IRAS80....	4–16	1.87 ± 0.21 (0.32)	4.00 ± 1.23 (1.14)	3.41 ± 2.11 (1.22)	24 ± 34 (23)
Average....	2–20	1.80 ± 0.04 (0.02)	3.97 ± 0.06 (0.14)	2.22 ± 0.16 (0.30)	9.2 ± 1.5 (3.9)

TABLE 6*b*

IRAS Results, Redshift Space

Sample	R (Mpc)	γ	s_0 (Mpc)	S_3	S_4
IRAS45....	3–9	1.36 ± 0.23 (0.23)	5.37 ± 1.23 (1.20)	2.28 ± 0.41 (0.25)	8.8 ± 3.4 (2.2)
IRAS55....	4–10	1.50 ± 0.17 (0.15)	4.65 ± 0.90 (0.79)	1.93 ± 0.21 (0.33)	6.6 ± 1.5 (2.8)
Average....	3–10	1.44 ± 0.09 (0.14)	4.90 ± 0.45 (0.73)	2.07 ± 0.23 (0.26)	7.5 ± 1.4 (2.1)

TABLE 7

Results for $\Omega^{4/7}/b$

Sample	$r_{\max}$ (Mpc)	$\xi_2(r_{\max})$	$\Omega^{4/7}/b$ (r_0)	$\Omega^{4/7}/b$ ($r_{\max}$)
CfA50	5.18	0.53	0.48 ± 0.24	0.63 ± 0.26
CFA65	5.52	0.83	-0.10 ± 0.79	-0.16 ± 0.78
CfA80	9.75	0.57	0.33 ± 0.44	0.43 ± 0.47
CfA90	11.3	0.22	0.48 ± 1.45	0.98 ± 1.61
CfA Average	—	—	0.41 ± 0.10	0.53 ± 0.15
SSRS50	4.73	0.64	0.58 ± 0.35	0.73 ± 0.41
SSRS65	7.44	0.58	0.92 ± 0.23	1.24 ± 0.31
SSRS80	7.91	0.58	0.99 ± 0.52	1.19 ± 0.57
SSRS90	8.79	0.36	1.07 ± 0.82	1.59 ± 0.90
SSRS Average . . .	—	—	0.85 ± 0.10	1.10 ± 0.16
IRAS45	7.04	0.32	0.71 ± 0.56	1.27 ± 0.64
IRAS55	7.60	0.33	0.32 ± 0.46	0.57 ± 0.50
IRAS Average . . .	—	—	0.48 ± 0.25	0.84 ± 0.45

Table 8
Estimates for S_3 and S_4

Reference	Sample	S_3 or $3Q_3$	S_4 or $16Q_4$
Groth & Peebles 1977 ...	Lick-Zwicky	3.9 ± 0.6	—
Fry & Peebles 1978	Lick-Zwicky	—	46 ± 8
Szapudi et al. 1992	Lick	4.3 ± 0.2	31 ± 5
Peebles 1980	CfA	2.4 ± 0.2	—
This paper	CfA	2.0 ± 0.3	6.3 ± 1.6
This paper	SSRS	1.8 ± 0.2	5.4 ± 2.2
Meiksin et al. 1992	IRAS	2.2 ± 0.2	10 ± 3
This paper	IRAS	2.2 ± 0.3	9.2 ± 3.9
Gaztañaga 1992	CfA (redshift)	1.9 ± 0.1	4.1 ± 0.6
This paper	CfA (redshift)	1.9 ± 0.2	5.1 ± 1.3
Gaztañaga 1992	SSRS (redshift)	2.0 ± 0.1	5.0 ± 0.9
This paper	SSRS (redshift)	1.8 ± 0.2	5.2 ± 1.3
Bouchet *et al.* 1993	IRAS (redshift)	1.5 ± 0.5	4.4 ± 3.7
This paper	IRAS (redshift)	2.1 ± 0.3	7.5 ± 2.1

6 Figure Captions

Fig. 1.—Average correlation function, $\bar{\xi}_2$ for each sample in the CfA (*a*), SSRS (*b*) and IRAS (*c*) catalogue. Open squares correspond to $\bar{\xi}_2$ for spherical (redshift) cells as a function of the radius R of the cell. Filled triangles correspond to $\bar{\xi}_2$ for conical (real space) cells as a function of the radius θz at the base of the cone. The dashed lines are the best power-law fit weighted by the errors.

Fig. 2.—Values of $\bar{\xi}_3$ (triangles) and $\bar{\xi}_4$ (squares), as a function of $\bar{\xi}_2$ for spherical (redshift) cells. There is one graph for each sample in the CfA (*a*), SSRS (*b*) and IRAS (*c*) catalogue. The dashed lines are the hierarchical law: $\bar{\xi}_J = S_J \bar{\xi}_2^{J-1}$ where S_3 and S_4 are fitted with the data weighted by the errors.

Fig. 3.—Values of $\bar{\xi}_3$ (triangles) and $\bar{\xi}_4$ (squares), as a function of $\bar{\xi}_2$ for conical (real space) cells. There is one graph for each sample in the CfA (*a*), SSRS (*b*), and IRAS (*c*) catalogue. The dashed lines are the hierarchical law: $\bar{\xi}_J = S_J \bar{\xi}_2^{J-1}$ where S_3 and S_4 are fitted with the data weighted by the errors.

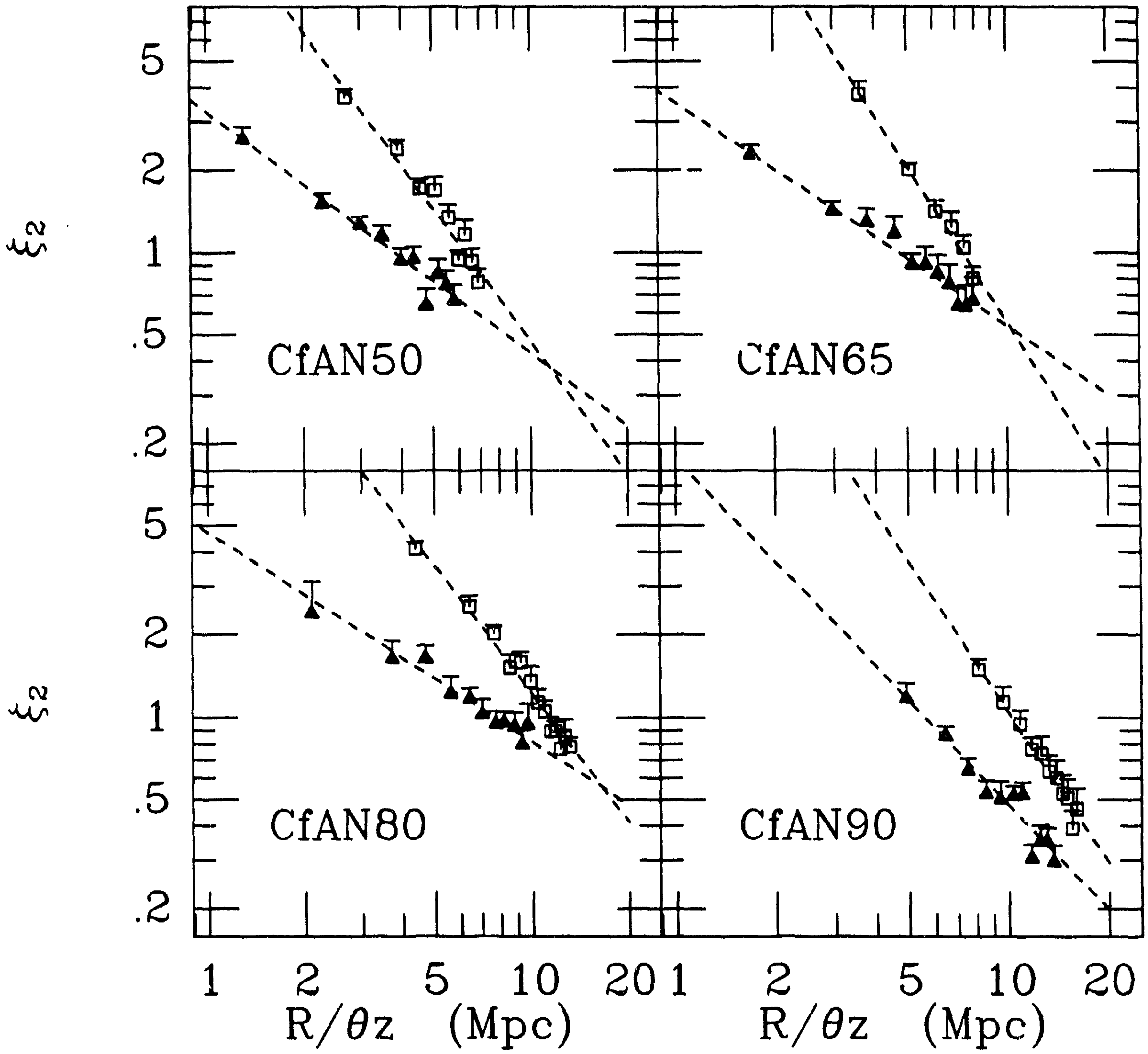

Figure 1*a*

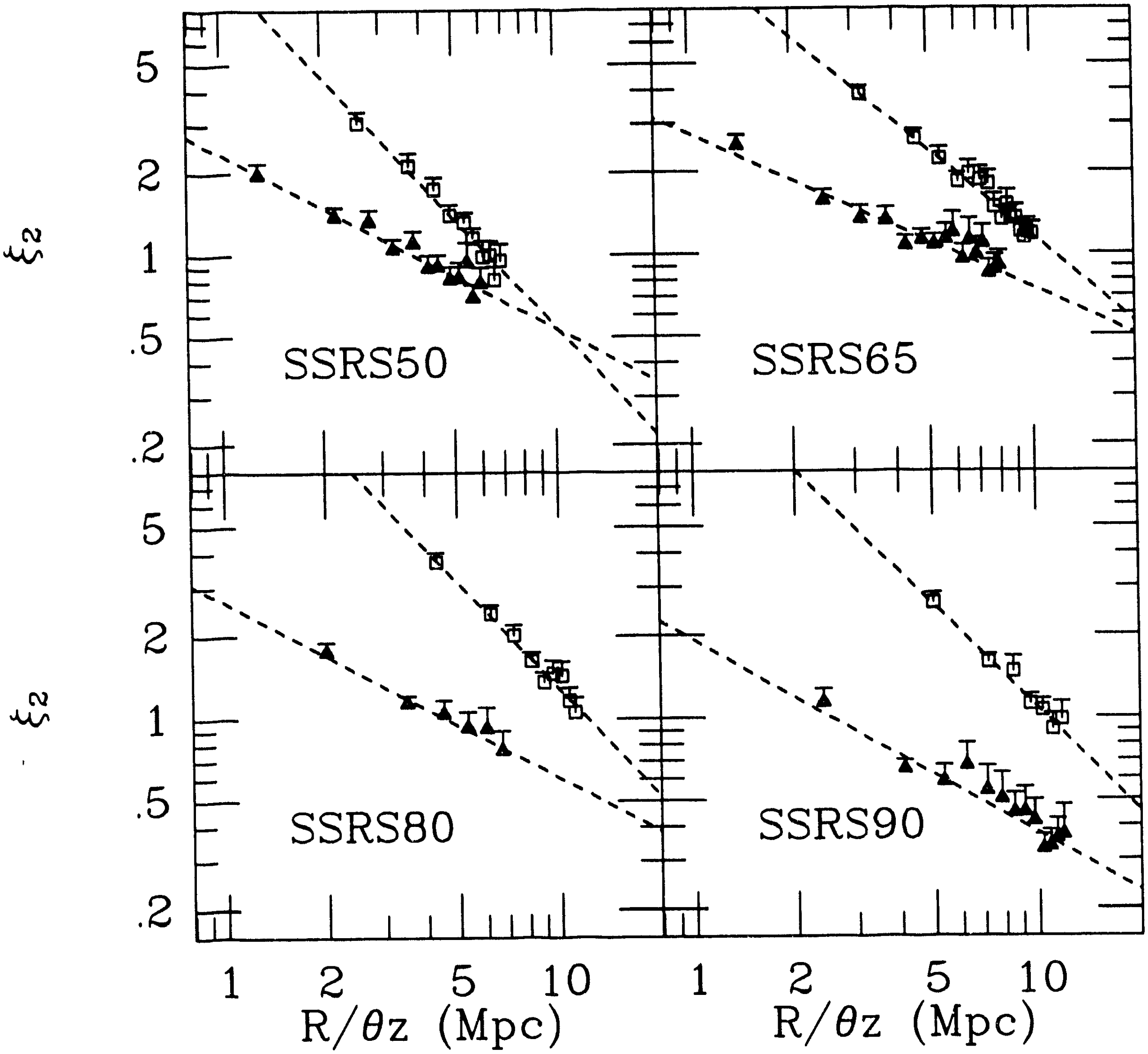

Figure 1*b*

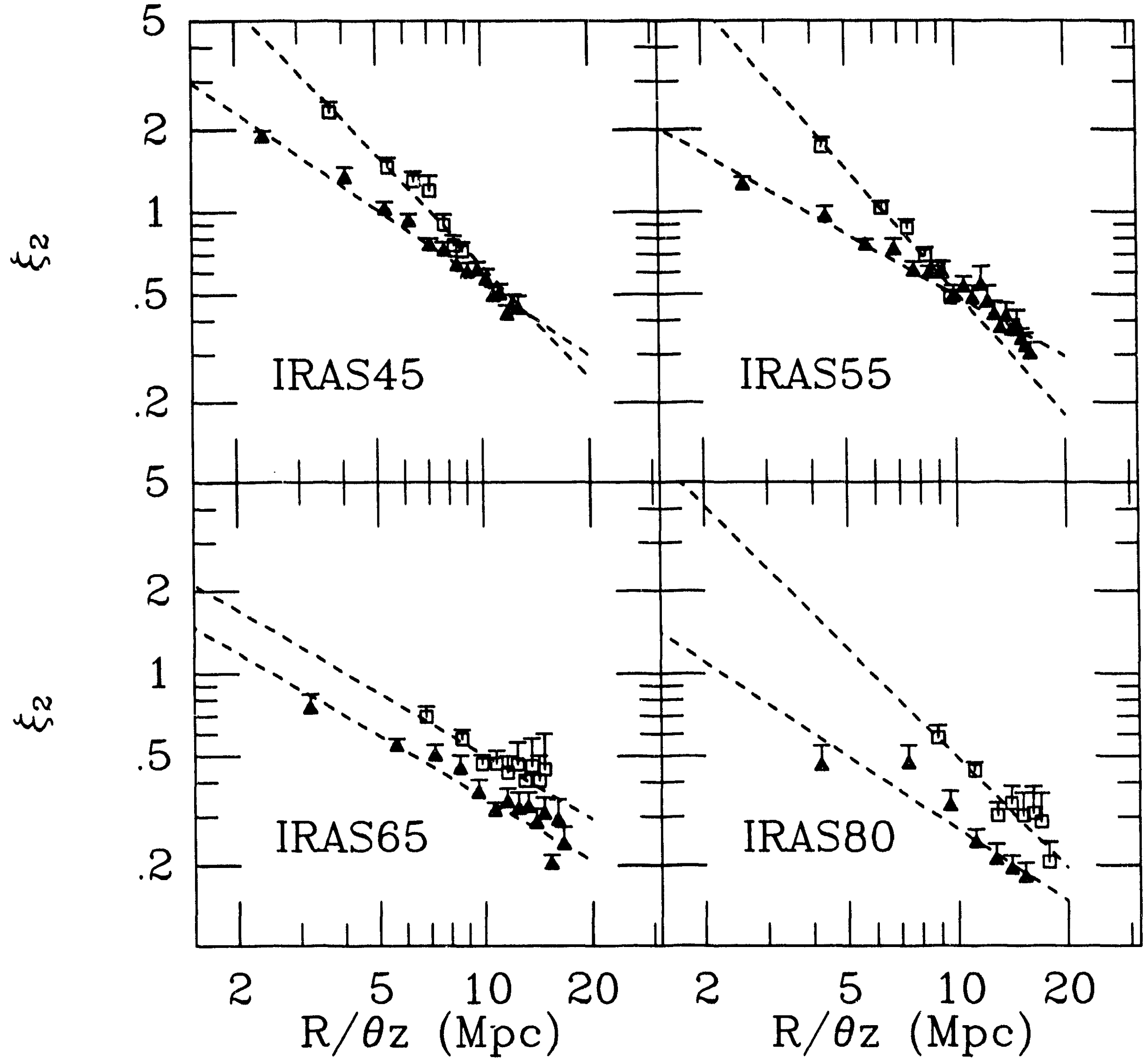

Figure 1*c*

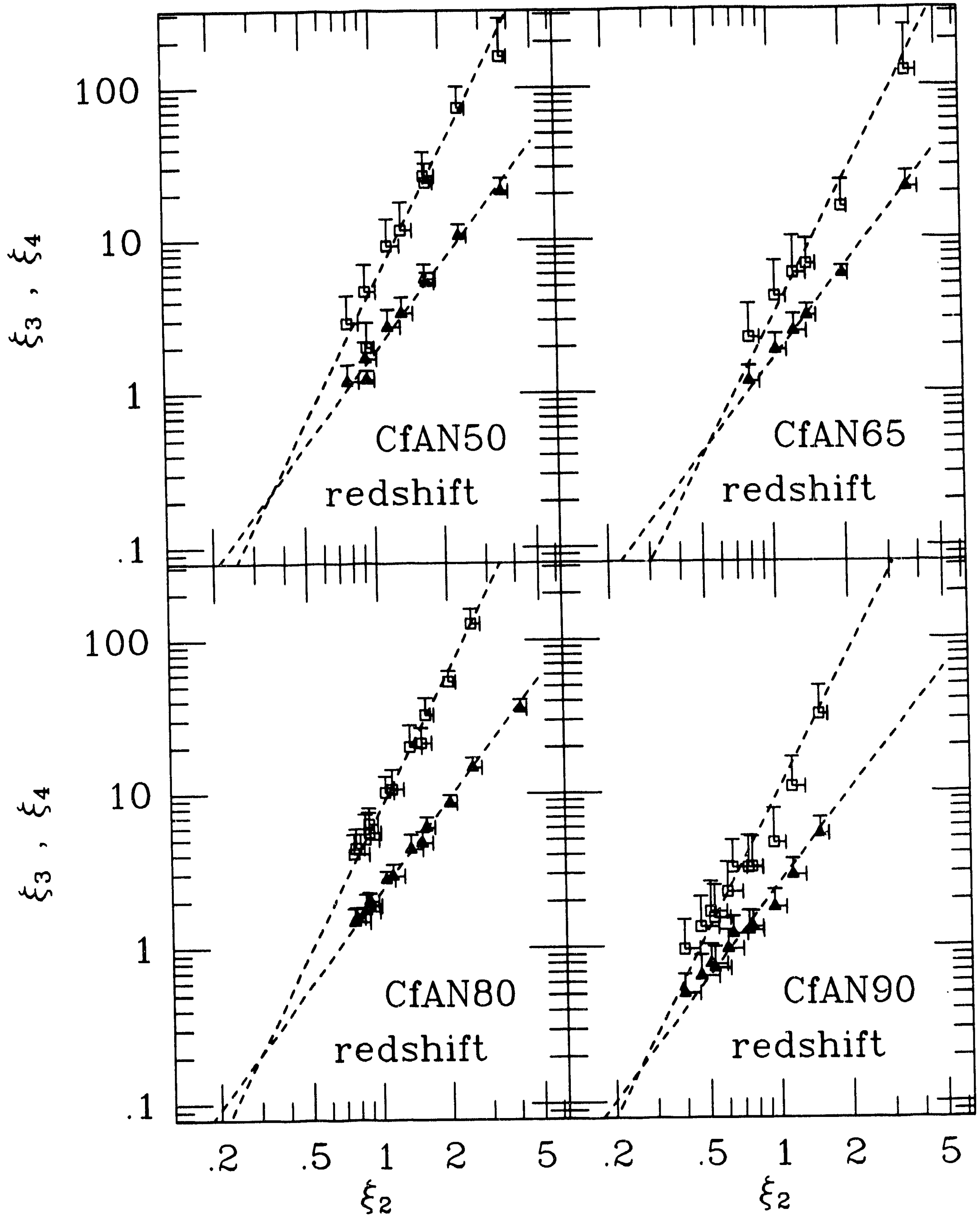

100
10
1
.1
100
10
1
.1
ξ_3 , ξ_4
ξ_3 , ξ_4
CfAN50
redshift
CfAN65
redshift
CfAN80
redshift
CfAN90
redshift
.2
.5
1
2
5
.2
.5
1
2
5
ξ_2
ξ_2

Figure 2*a*

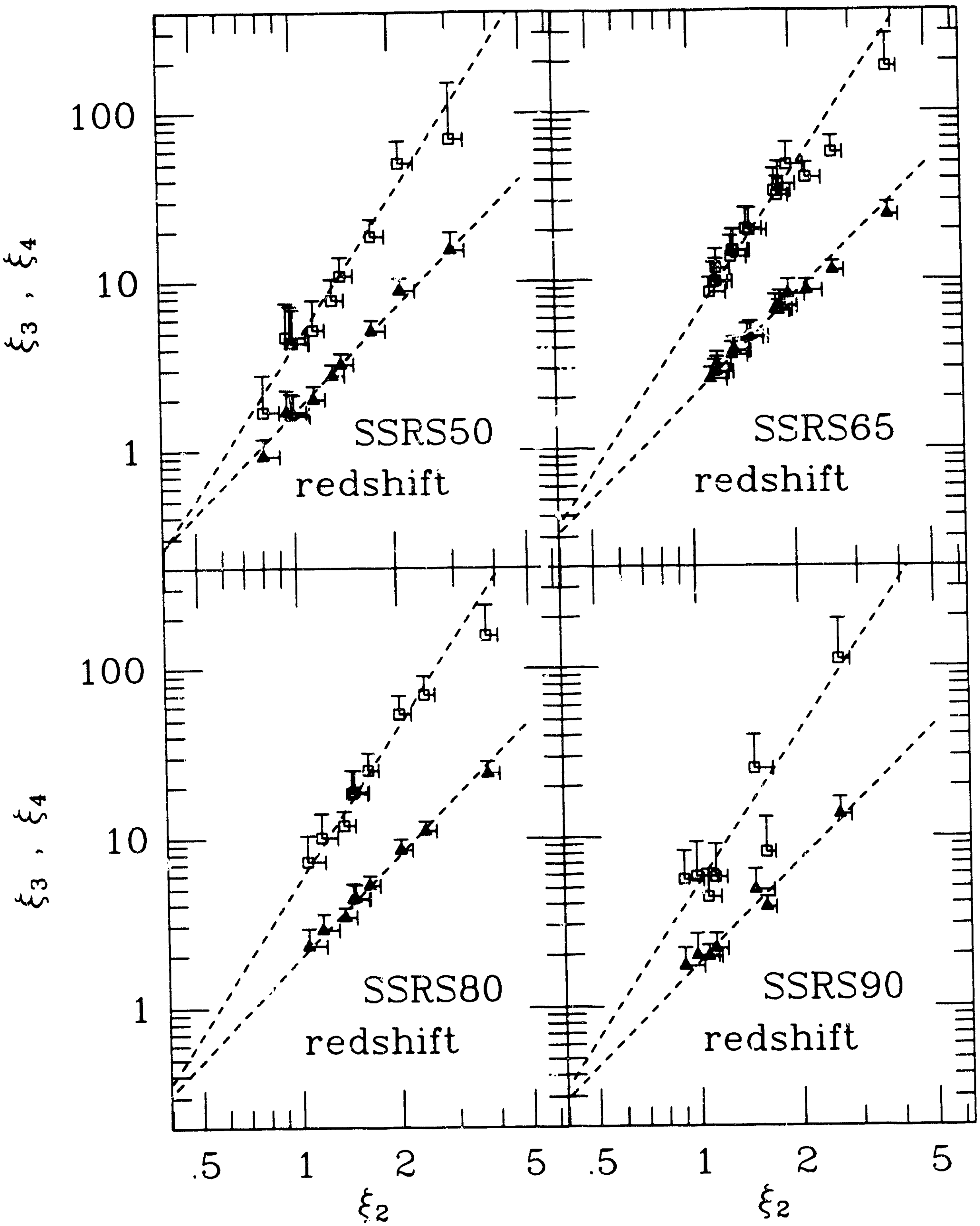
100
10
1
ξ_3 , ξ_4
SSRS50
redshift
SSRS65
redshift
SSRS80
redshift
SSRS90
redshift
.5
1
2
5
ξ_2

Figure 2*b*

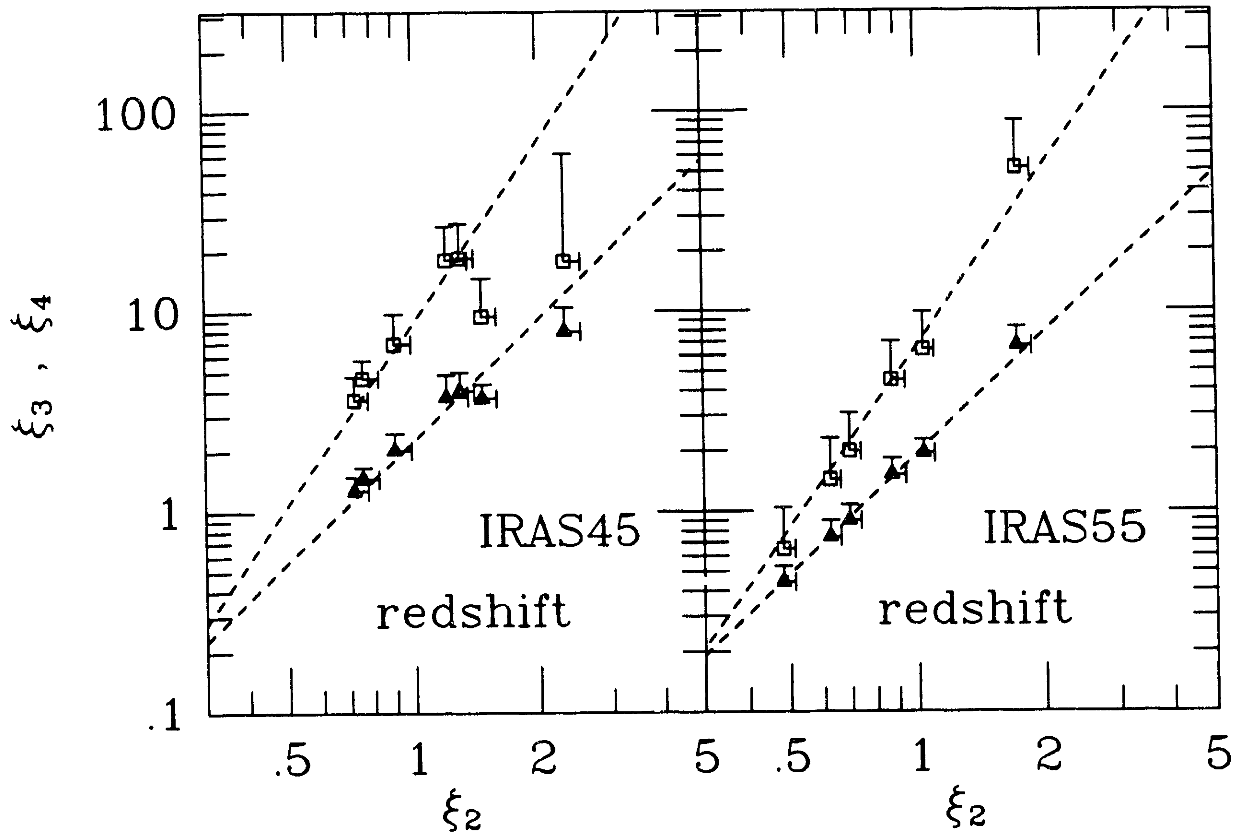
100
10
1
.1
ξ_3 , ξ_4
.5
1
2
5
.5
1
2
5
ξ_2
ξ_2
IRAS45
redshift
IRAS55
redshift

Figure 2*c*

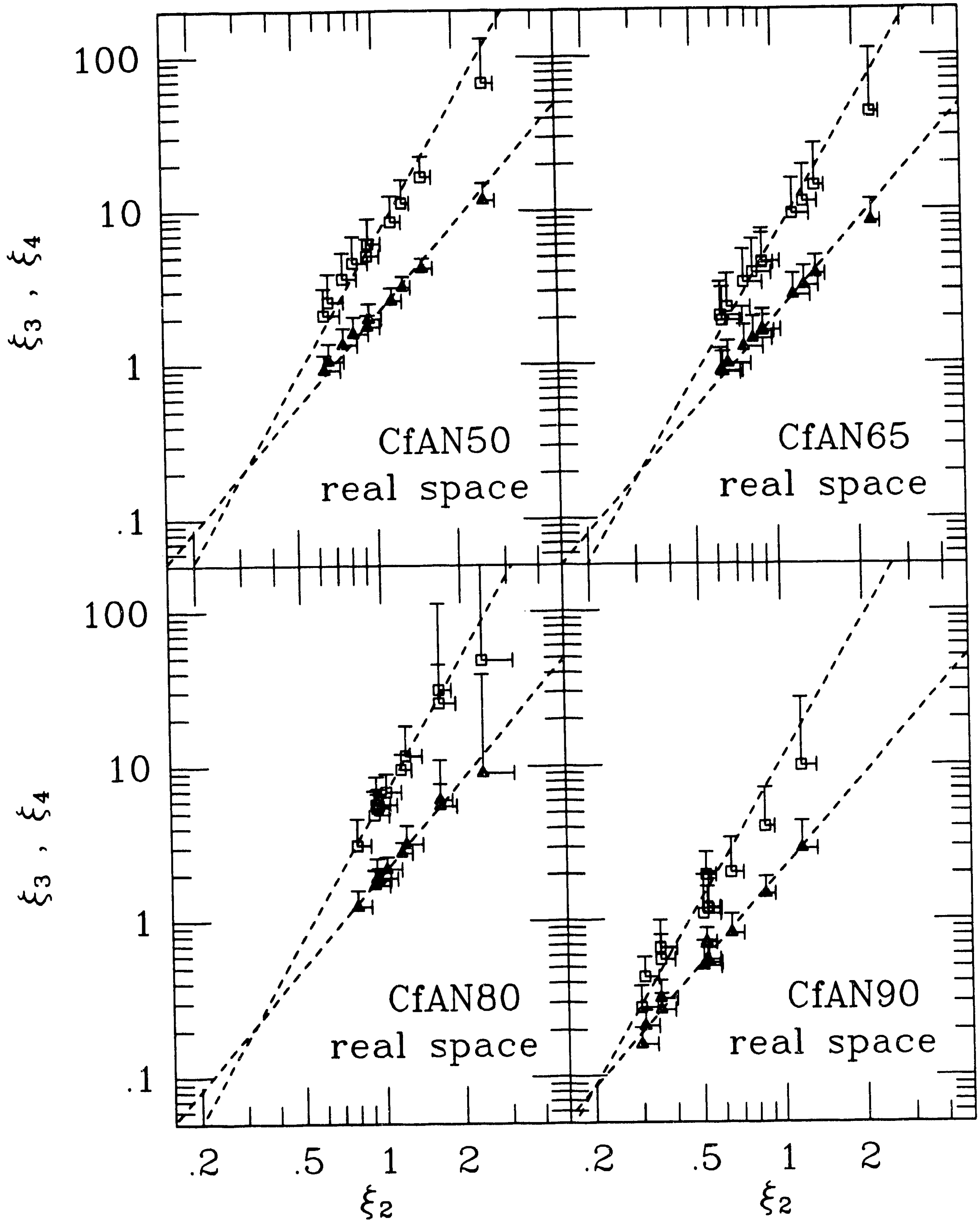

100
10
1
.1
ξ_3 , ξ_4
CfAN50
real space
CfAN65
real space
100
10
1
.1
ξ_3 , ξ_4
CfAN80
real space
CfAN90
real space
.2
.5
1
2
ξ_2
.2
.5
1
2
ξ_2

Figure 3*a*

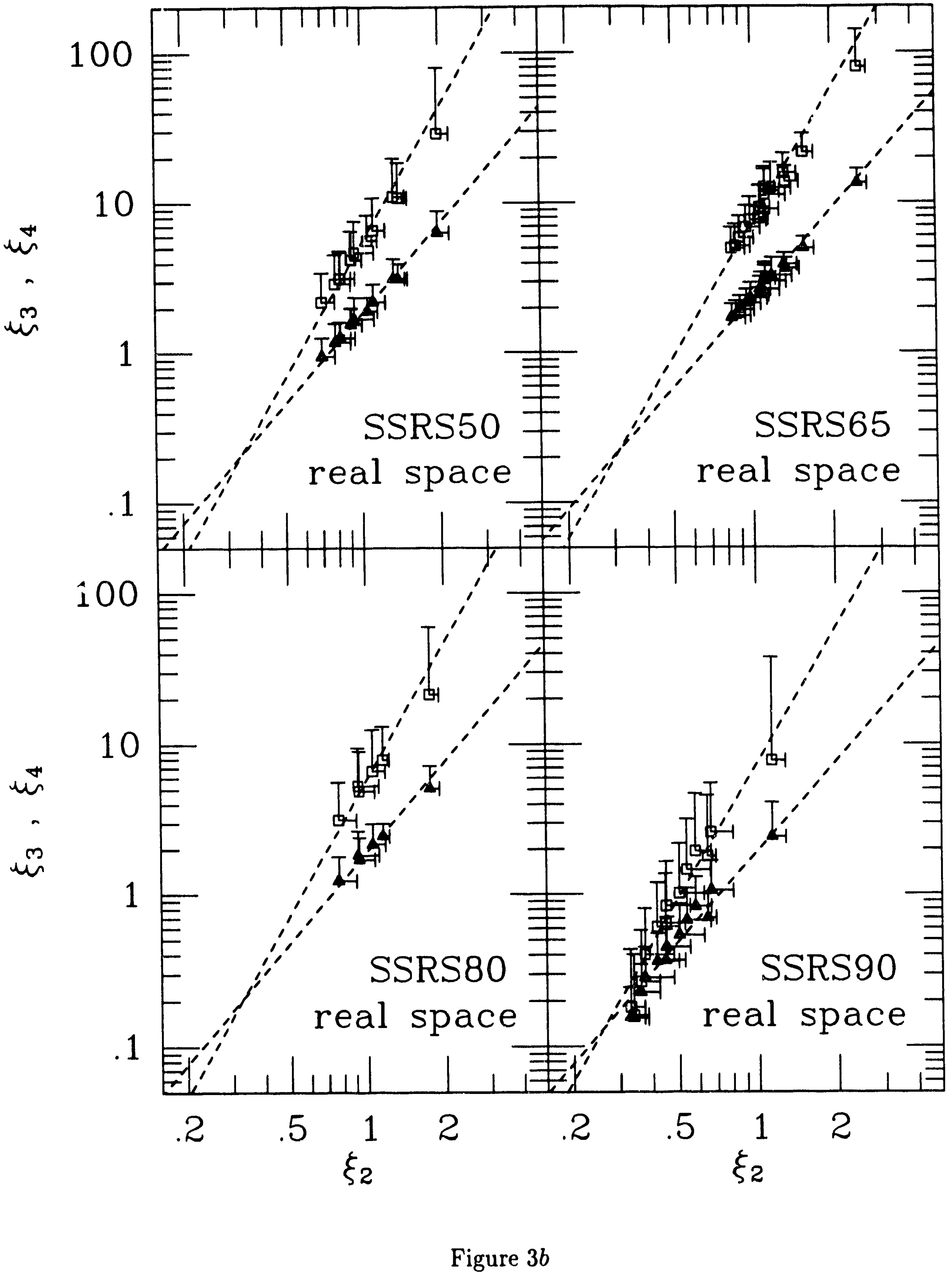

100
10
1
.1
ξ_3 , ξ_4
SSRS50
real space
SSRS65
real space
SSRS80
real space
SSRS90
real space
.2
.5
1
2
ξ_2

Figure 3*b*

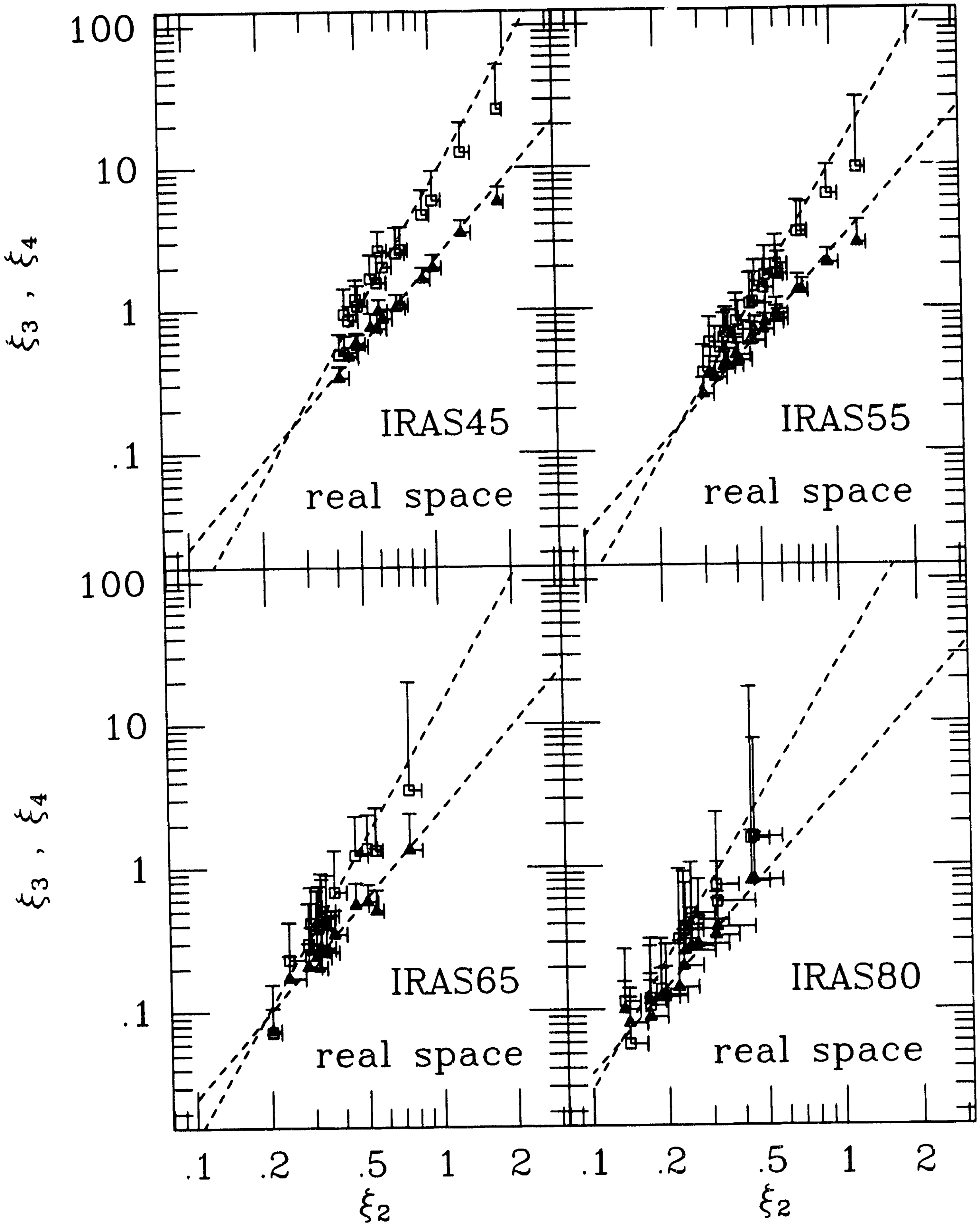

100
10
1
.1
ξ_3 , ξ_4
IRAS45
real space
IRAS55
real space
100
10
1
.1
ξ_3 , ξ_4
IRAS65
real space
IRAS80
real space
.1
.2
.5
1
2
.1
.2
.5
1
2
ξ_2
ξ_2

Figure 3*c*

DATE
FILMED

8/4/93

END